Journal of Ovonic Research Vol. 21, No. 1, January - February 2025, p. 37 - 45

Photoluminescent, optical and magnetic property characterization of green chemistry method prepared calcium doped ZnO nanoparticles

R. J. Ramalingam [a,*], K. K. Sadasivuni [b], H. Allohedan[a], M. Sunderajan [c], S. Yuvaraj [c]

[a] *Department of chemistry, College of science, King Saud University, P.O. Box 2455, Riyadh 11451, Saudi Arabia*

[b] *Department of Mechanical Engineering, Inha University, Incheon,South Korea*

[c] *Department of Physics, Paavendhar College of Arts & Science, Salem - 636121, India*

Employing a green synthesis technique, we produce cost-effective zinc oxide nanoparticles and calcium-doped zinc oxide nanoparticles by utilizing Citrus sinensis fruit extract as an efficient reducer and encapsulating agent. XRD analysis confirmed a wurtzite structure for the as synthesized ZnO and calcium doped ZnO nanoparticles. Oxidation states and quantification of the element on the surfaces of pure and Ca-ZnO was achieved through XPS investigations. Nano-flakes structures of the synthesized samples are prominently depicted in the HR-SEM image, providing visual insight into their morphology. The elemental analysis and their quantity were discerned using EDX spectrum. Moreover, Magnetization–Field (M–H) hysteresis curves demonstrated diamagnetic behavior at room temperature.

(Received September 15, 2024; Accepted January 13, 2025)

Keywords: Zinc oxide, Optical behavior, Magnetic properties, Calcium doped ZnO

1. Introduction

Particles at nano region have garnered significant attention across various fields due to their distinct magnetic, surface, optical and structural properties compared to their bulk counterparts. Zinc oxide (ZnO) nanoparticles, characterized by a wide direct band gap and substantial exciton binding energy, such as 3.36 eV and 60 meV. Various method prepared ZnO and its doped counterpart could act as a versatile material with applications spanning antibacterial agents, OLEDs, window layers in solar cells, UV radiation absorption, heterogeneous catalysis, electrical resistance, surface acoustic wave equipment fabrication, cosmetic coloring, semiconductor devices, sensors, catalysis and spintronics [1-7].

Researchers are delving into the unique characteristics of ZnO for these applications, recognizing its potential for further enhancement in electrical and optical properties through metal element doping [8,9]. Doping ZnO with various metal elements is a common strategy to tailor its properties for optoelectronic device fabrication [10]. Early studies by Geetha D et al. (2016) and Umaralikhan (2017) demonstrated that the optical property performance of pristine inner component could be significantly improved by reducing defect sites through doping [11-15].

While there are numerous techniques for producing nanoparticles, our primary emphasis is on the eco-conscious green chemistry synthesis method. Emphasizing sustainability and environmental friendliness, the green synthesis technique stands out [14]. Within this method, we opt for Psidiumguajava fruit (PGF) extract as our preferred means for nanoparticle synthesis. It's important to highlight the diverse composition of the PGF skin, encompassing essential compounds such as flavonoids, quercetin, guaijavarin, morin-3-O-L-lyxopyranoside, oleanolic acid, saponin, calcium, phosphorus, iron and Vitamin A, C [15, 16]. The phenolic compounds contained within PGF demonstrate promise in halting the progression of cancerous cells and preventing premature aging in the skin of young individuals.

---

[*] Corresponding author: jrajabathar@ksu.edu.sa

https://doi.org/10.15251/JOR.2025.211.37

The synthesis of pure and Ca doped ZnO in this work involved the use of plant extract as a capping and reducing mediator, reflecting a commitment to ecofriendly low cost adopting green synthesis methodologies. The fabricated materials underwent thorough examination, particularly concerning their thermal, optical and structural attributes, with a specific emphasis on pure and Ca-doped ZnO compositions. During optical examination, it was observed that both CZNP and ZNP samples exhibited a reduction in defect levels. Notably, the Ca doped ZnO sample displayed the highest optical properties among the two. Further, the surface property and magnetic property of as prepared Ca-ZnO nanoparticle have been studied in detail.

2. Experimental

2.1. Preparation of citrus sinensis extract extracts

After adding 25 grams of newly diced Citrus sinensis extract bits into 200 milliliters of deionized water, the blend underwent a heating process for 20 minutes at 60°C. Subsequent filtration was followed by the careful transfer of the solution into a 250 mL flask.

2.2. Green synthesis of calcium doped ZnO nanoparticles

In the process of synthesizing the ZnO sample, the first step involved the creation of a solution exhibiting a brown hue similar to that of the Citrus sinensis extract. This required the blending of 100 milliliters of citrus extract with a solution containing 0.1 mole of zinc (II) nitrate hexahydrate. Afterwards, the solution was subjected to stirring for 3 to 4 hours at 70°C. Ultimately, calcination at 700°C for 2 hours was carried out to produce Calcium doped and undoped ZnO nanoparticles with good crystalline property [14]. In order to fabricate the Ca-doped ZnO nanoparticles, by following process: Initially, we blended 100 ml of the Citrus sinensis extract solution with 100 mL of zinc (II) nitrate and calcium nitrate (0.95 and 0.05 moles, respectively) to obtain a solution characterized by its brown tint [14]. Afterward, the solution was stirred for a period of 3 to 4 hours at 70°C, and subsequently underwent calcination at 700°C for 2 hours, resulting in the generation of Ca-doped ZnO nanoparticles. Designations ZNP and CZNP are assigned to the prepared ZnO and Ca-doped ZnO.

2.3 Characterization

Employing an X-ray diffractometer, specifically the X'PERT PRO analytical model, the produced samples were analyzed. Recorded between 20° and 80°, diffraction patterns of the synthesized materials were captured using monochromatic light with a wavelength (λ) of 1.54Å. SEM coupled with EDAX for elemental composition analysis was conducted using an FEI-QUANDA 200F microscope at 30 kV. The FT-Raman spectra were acquired utilizing a Burker RFS 25 spectrometer. Photoluminescence (PL) analysis within the 450-600 nm wavelength range was conducted using Jovin YvonFlurolog-3-11 spectrometer. Investigation of magnetization curves at room temperature was carried out employing a PMC Micro Mag 3900 type VSM, and a 1 Tesla magnet.

3. Results and discussion

3.1. X-ray diffraction characterization of ZnO and CZN

Within the 2θ range of 20° to 85° at ambient temperature, the powder XRD captured diffraction patterns of pure and Ca-incorporated ZnO particles at nano region (Fig. 1a). These patterns exhibited characteristic peaks consistent with a hexagonal wurtzite structure, as supported by JCPDS Card No: 792205. Crucially, no impurity phases were identified, indicating that the structure of ZnO was unaltered by the introduction of calcium ions.

Furthermore, Bragg's law was employed to analyze the XRD pattern of pure and Ca-incorporated ZnO system. The significant Bragg reflection planes for pure ZnO NPs were detected at 2θ values of 31.6°, 34.4°, and 36.2°, representing the (100), (002), and (101) crystallographic planes, respectively. Likewise, peaks obtained at 2θ values of 31.7°, 34.3°, and 36.2° were attributed to the (100), (002), and (101) planes of Ca-doped ZnO nanoparticles [16,17].

Equation (1) facilitated the calculation of lattice parameters for both pure and Ca-incorporated ZnO samples, utilizing their respective X-ray diffraction patterns.

$$\frac{1}{d^2} = \frac{4}{3}\left(\frac{h^2 + hk + k^2}{a^2}\right) + \frac{l^2}{c^2} \tag{1}$$

In Fig. 1b, the diffraction peaks' maximum intensity undergoes a shift towards lower angles following Ca^{2+} doping, indicating an enlargement in lattice constants a (b) and c from 3.248 to 3.250 Å and 5.205 to 5.211 Å, respectively. This expansion of the lattice might stem from the small replacement of the higher ionic radii of Ca^{2+} (rCa^{2+} = 0.099 nm) with the lower ionic radii of Zn^{2+} (rZn^{2+} = 0.074 nm). Conversely, the introduction of calcium at the Zn sites alter the ionic radii and induce changes in the inter-atomic distance (‘d’), giving rise to a shift towards lower angles [18].

Average nano-crystalline sizes for both the pure and Ca-doped ZnO samples were derived using equation (2) [19, 20].

$$D = \frac{k\lambda}{\beta \cos\theta} \tag{2}$$

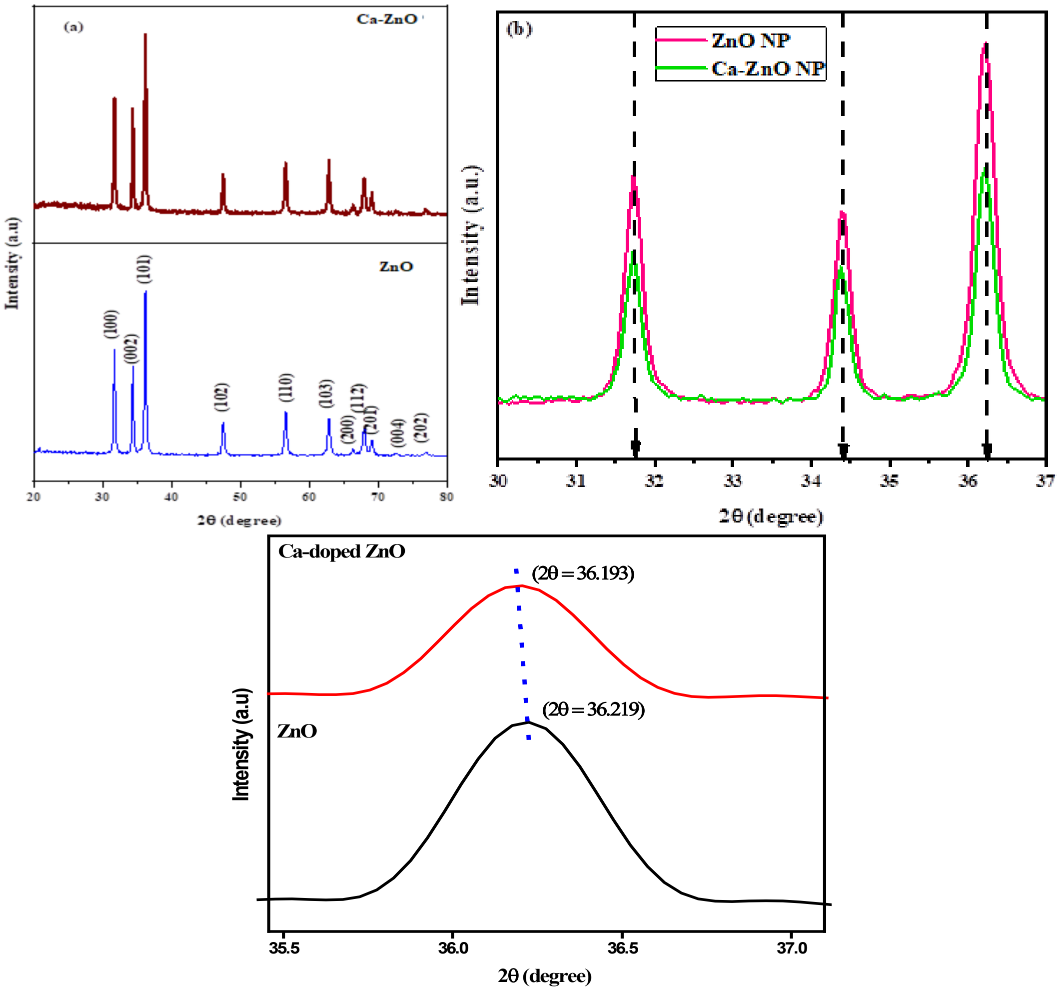

Fig. 1. (a) X-ray diffraction pattern of ZnO NP and Ca-ZnO NP samples; (b) X-ray diffraction pattern of ZnO and Ca-ZnO NP at focused region; (c) XRD peak shift of ZnO and Ca doped ZnO nanoparticles.

Within the equation, a constant parameter known as k is employed, maintained at a value of 0.89. Furthermore, it includes the X-ray wavelength at 0.154 Å and the diffraction angle (θ) according to Bragg's law. Parameter β describes the extent of the diffraction peaks' width at half of the maximum intensity, characterizing the synthesized nanomaterials. By applying Scherrer's equation, we established the average crystallite size of pure and Ca doped ZnO to be 40-37 nm, respectively [21, 22], confirming the nanoscale properties of the prepared sample. We clearly noticed a shift in the peak towards the lower angle, as the doping concentration of Ca^{2+} ions increased as the ionic radii of Ca^{2+} ions is higher than Zn^{2+} ions in Fig. 1c. Moreover, the evaluation revealed that the average size of crystalline for the Ca doped ZnO sample is smaller in comparison to that of the ZnO sample. This reduction in size is attributed to the modulation exerted by the dopant Ca^{2+} ions on the growth and nucleation processes of the primary sample (ZnO) [13, 14].

3.2. X-ray photoelectron spectroscopy (XPS) study of as prepared ZnO and Ca-ZnO nanoparticles

In order to gain a deeper understanding of the oxidizing states, surface chemical elements, valence information, and chemical composition of both pure and Ca-substituted ZnO nanoparticles, an XPS analysis was conducted. Fig. 2 illustrates the presence of elements such as Ca, Zn, and O in the wide spectrum of XPS.

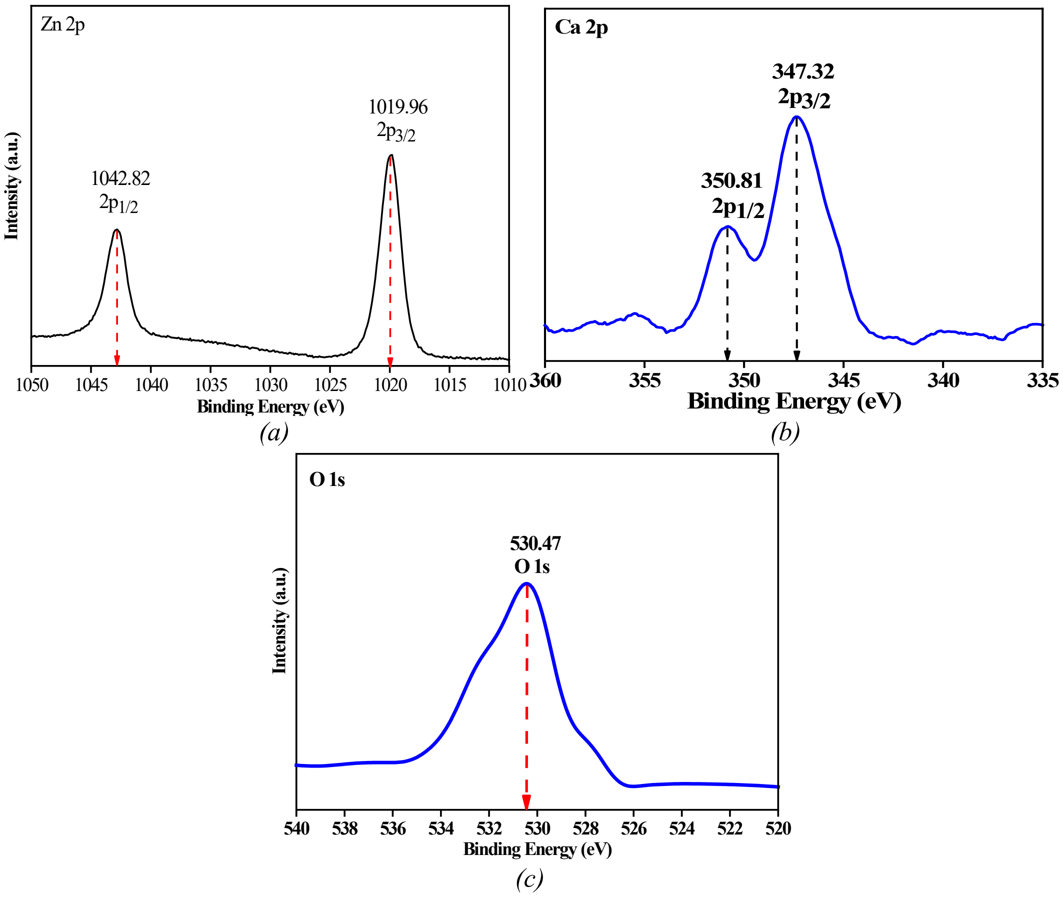

(a) *(b)* *(c)*

Fig. 2. (a) XPS spectra of Zn 2P; (b) XPS spectra of Ca 2P; (c) XPS spectra of O1s.

The Zn 2p binding energy peaks at 1042.82 eV for Zn 2P$_{1/2}$ and 1019.96 eV for Zn 2P$_{3/2}$, indicating the presence of vacancies associated with the oxidation state. This data suggests that charge transfer processes may involve Zn^{2+}. In Figure 2, the peaks observed at 350.81 eV in the Ca 2p spectrum correspond to Ca 2p1/2, while the peak at 347.32 eV are related to Ca 2p3/2. These peaks indicate the separation between the two energy levels and suggest the presence of calcium in the 2+ oxidation state. The higher number of vacancies in the ZnO and Ca-substituted ZnO sample is thought to be the reason behind this occurrence. This is because when Zn^{2+} is replaced by Ca^{2+}, it can lead to the creation of oxygen vacancies to balance the overall charge maintenance. In the O 1s binding energy spectra, there is a peak at 530.47 eV, which is believed to be caused by the presence of metal-oxygen (O2-) and OH- groups on the metal oxide surface. In addition, the oxygen spectrum (O 1s) revealed the following existence of oxygen imperfections, oxygen atomic orientations, and chemisorbed ions within the ZnO matrix. The XPS analysis has provided evidence supporting the formation of both pure and Ca-doped ZnO samples. These samples were synthesized using a green method that employed PGF extract [25, 26].

3.3. Scanning electron microscopy (SEM) and energy-dispersive X-ray analysis

The transformation of surface morphology in both pure and Ca-substituted ZnO samples during synthesis is captured in Fig. 3. Nano-scale grains, in conjunction with nano-flakes and/or flower-shaped nanostructures, were identified through SEM analysis of the fabricated nanoparticles. The grain sizes of ZnO and Ca doped ZnO nanoparticles were determined via SEM analysis, the measured particle size between 47 to 57 nm. The decrease in grain size noted in doped nanoparticles compared to their pure counterparts is ascribed to the distortion induced by Calcium ions on the ZnO surface during the doping process. It is worth mentioning that the grain sizes derived from SEM exhibit slight variation from those obtained through X-ray diffraction. This discrepancy might be due to the different measurement methodologies: SEM evaluates the size of aggregated clusters, whereas XRD determines the domain size in ZnO and Ca-doped ZnO. Furthermore, the EDX analysis was conducted to determine the elemental composition of pure and Ca-doped ZnO samples, as demonstrated in Table 1. Both pure and Ca-doped ZnO nanoparticles displayed peaks corresponding to Ozygen (O), Calcium (Ca) and Zinc (Zn). The composition of the materials in terms of atomic and weight percentages is provided in Table 1.

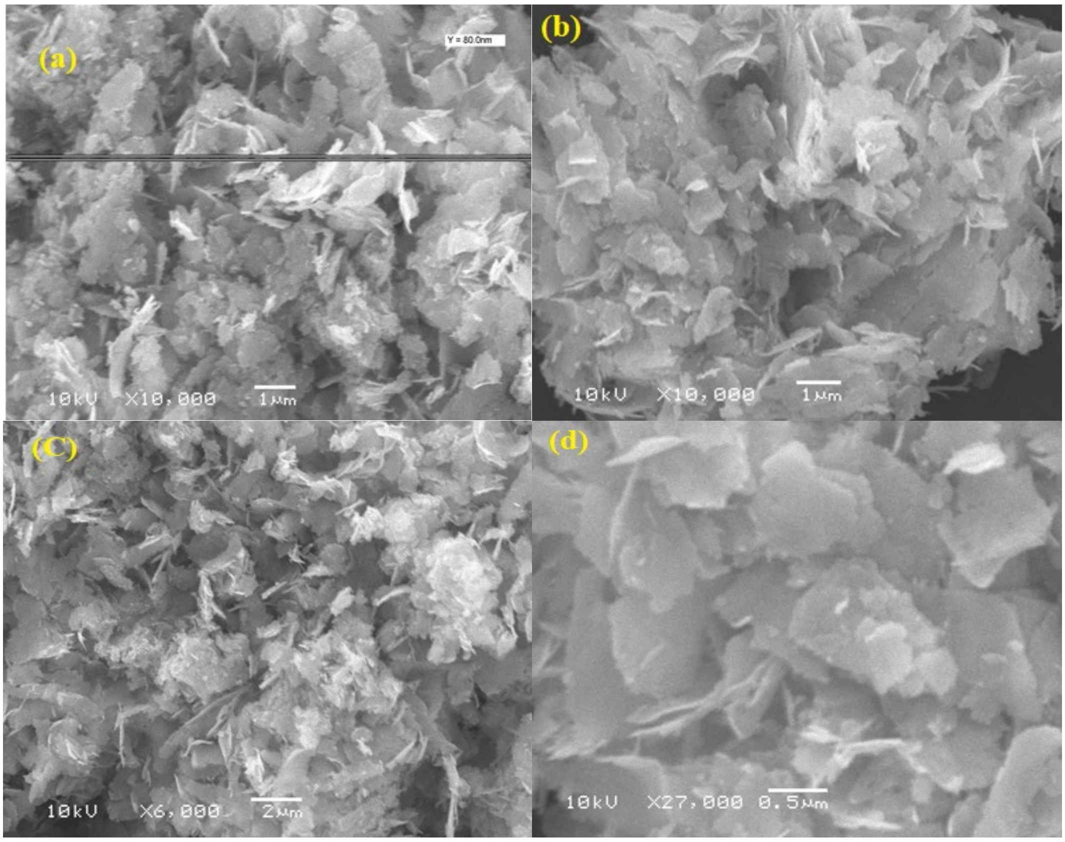

Fig. 3. (a-d) SEM images of Calcium doped ZnO at various magnification.

Table 1. The elemental composition of ZnO NP and Ca-ZnO nanoparticles.

Sample Code	Zn	O	Amount of Ca doping (%)
ZnO NP	43.3	56.7	-
Cc-ZnO ZNP	44.4	53.7	1.9

3.4. Fourier infrared raman spectroscopy analysis of doped and undoped Ca-ZnO nanoparticles

Raman spectroscopy serves as a vital method for delving into photon and phase transition boundaries. The wavenumber versus Raman intensity graphs for pure and Ca-doped ZnO samples are depicted in Figure 4(a-b). Within a simple ZnO unit cell, all four atoms are located at the C3v site, resulting in a total of 12 phonon branches, consisting of nine optical and three acoustic modes. Analysis of ZnO phonon dispersion relation at the Brillouin zone center (q=0) reveals these 12 branches, which are further classified into distinct phonon modes.

$$\Gamma = 2(A_1+B_1+E_1+E_2)$$

In this context, acoustic modes are denoted by Γacous. = A_1+E_1, while optical modes are indicated by Γopt. = $A_1+2B_1+E_1+2E_2$. The B_1 mode remains inactive, with the remaining modes showing Raman activity. Phonons characterized by E_1 and A_1 and symmetry undergo a split into longitudinal optical (LO) and transverse optical (TO) modes. Both IR and Raman activity are observed in these E_1 and A_1 phonon modes. Two non-polar vibration modes, E_2^{low} and E_2^{high}, constitute the E_2 phonons. The vibrations mode of the Zn sub-lattice mostly pertains to the lower frequency mode of E_2, while the other frequency mode E_2 corresponds to oxygen atoms. Despite its Raman activity, the E_2 non-linear mode does not elicit any response in the infrared spectrum. The 98 cm^{-1} peak in ZnO is associated with E_2^{low}, representing Zn sub-lattice vibrations. Conversely, in Ca-doped ZnO, the presence of Ca^{2+} ions induce a slight shift to 102 cm^{-1}. In both pure and Ca-doped ZnO samples, another Raman mode known as E_2^{high} is observed at 443 / 445 cm^{-1}, respectively, predominantly linked to oxygen vibration. The significant asymmetry of these peaks is largely attributed to lattice disorder and harmonic phonon to phonon interactions.

Both pure and Ca-doped ZnO samples exhibit the A_1 (LO) mode at 564 cm^{-1} and 571 cm^{-1}, respectively, while the E_1 (LO) mode is observed at 584 cm^{-1} for ZnO and 598 cm^{-1} for Ca-doped ZnO. These modes demonstrate comparable wavenumber and reveal an elevation from the background, potentially owing to second order Raman scattering. Both modes could be affected by the presence of Ca impurities, as the influence of phonons beyond the Brillouin Zone's core needs to be considered. The difference observed between E_2^{high} and E_2^{low} modes can be attributed to lower wavenumber range of second order mode, which registers at 341 cm^{-1} and 346 cm^{-1} respectively for ZnO and Ca-doped ZnO.

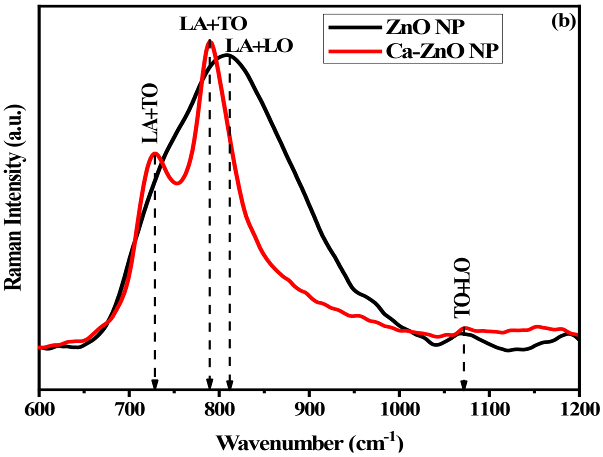

Fig. 4. FT-Raman spectra of ZNP and CZNP samples.

3.6. Photoluminescence (PL) spectra

At ambient temperature, both pure and Ca-doped ZnO exhibit photoluminescence spectra that are excited by 254 nm [29]. Fig. 5(a-b) illustrates the Gaussian peak fit of pure and Ca-doped ZnO samples, with the peaks of ZnO labeled U1-U6 and K1-K6, respectively. Fig. 7(a-b) displays the peak values separately. Utilizing photoluminescence emission spectra, the photon energy of synthesized samples is estimated, and the photon energies are presented in Fig. 5c.

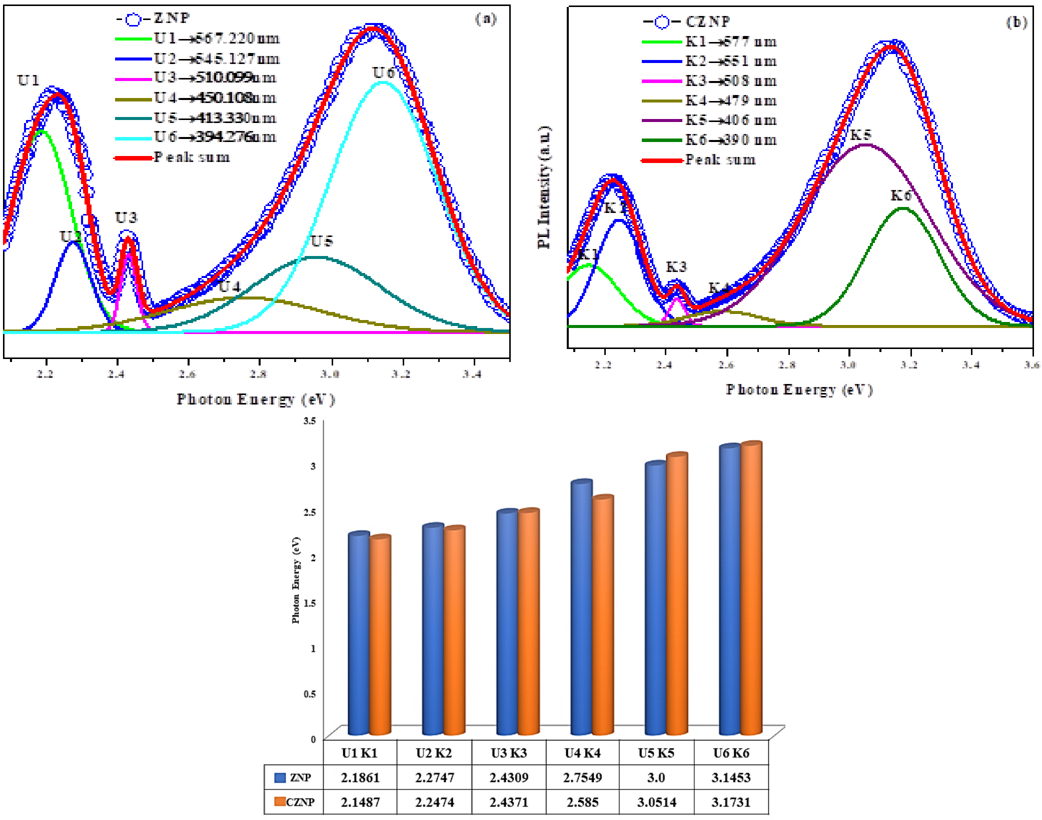

	U1 K1	U2 K2	U3 K3	U4 K4	U5 K5	U6 K6
🟦 ZNP	2.1861	2.2747	2.4309	2.7549	3.0	3.1453
🟧 CZNP	2.1487	2.2474	2.4371	2.585	3.0514	3.1731

Fig. 5. (a-c) Photoluminescent spectra of green synthesis method prepared ZnO and Ca-doped ZnO and its respective photoenergy values.

The UV emission observed at 3.14 eV is attributed to the near-band-edge emissions of recombination of excitonic transitions. The violet emission centered at 413.33 nm with 3.0 eV is ascribed to transition between defect sites in or interstitial oxygen at boundaries and at the valence band. A surface defect causes the blue emission with 2.7549 eV in ZNP at 450.108 nm [21]. The presence of an ionized oxygen vacancy on the surface and a defect in the zinc oxide lattice result in two green emissions centered at 510.099 nm with 2.4309 eV and 545.127 nm with 2.2747 eV [12]. Interstitial oxygen vacancies are responsible for the yellow emission detected at 567.220 nm with 2.1861 eV. In the photoluminescence spectrum of the CZNP sample, a slight red shift in the blue emission is observed compared to the ZNP sample result. This minor shift is attributed to the band tailing effect, which decreases the energy gap. Changes in the blue emission are induced by the presence of dopant ions on the zinc oxide lattice site.

3.7. Magnetic properties

VSM analysis was utilized to investigate zinc oxide and calcium-doped zinc oxide nanoparticles. The results, depicted in Figure 6, illustrate the relationship between magnetization (emu/g) and the applied field (Oe). It is evident from the graph (Fig. 6) both ZnO and calcium-doped ZnO demonstrate diamagnetic behavior for the as prepared nanoparticles. Remarkably, the coercivity value increases from 88.12 Oe to 137.06 Oe upon calcium doping in zinc oxide. Furthermore, there is an increase in the Mr and Ms values from 0.0014 to 0.016 emu/g and from 0.0026 to 0.049 emu/g due to certain factors like surface defects and cationic redistribution that affect the net magnetic moments, magnetic super-exchange interactions and random magnetic orientation, and lattice defects. The magnetic saturation and low retentivity may indicate magnetically pristine materials and the existence of defects. Within this system, diamagnetic behavior is influenced by the presence of oxygen vacancies and surface size as pivotal factors.

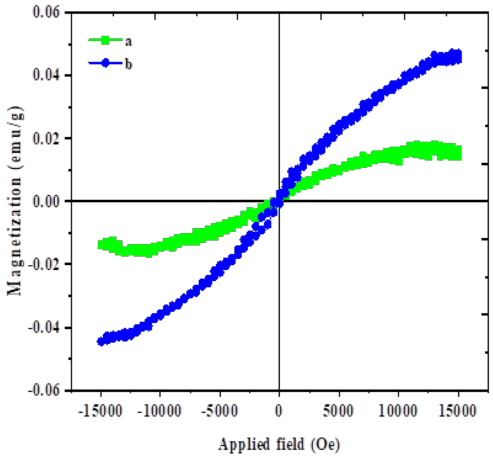

Fig. 6. Applied field versus magnetization of ZnO and Ca doped ZnO nanoparticles.

4. Conclusion

To encapsulate, ZNP and CZNP samples were created by employing PGF extract through environmentally conscious synthesis techniques. XRD examinations authenticated the hexagonal wurtzite configurations within the synthesized nanoparticles. The average dimensions of the crystallites were established at 40 nm for ZnO and 37 nm for Ca-doped ZnO samples. XPS analysis shed light on the surface properties and oxidation states of pure and Ca-doped ZnO samples. Meanwhile, HR-SEM images depicted nano-sized crystallized grains along with nano-sized flake and/or flower-structured nanoparticles. PL spectra demonstrated a blue emission shift due to the presence of Ca^{2+} ions within the zinc oxide lattice sites. Moreover, Ca-doped ZnO nanoparticles exhibited minor variations in photon energy, potentially influencing optical applications. Thermogravimetric analysis demonstrated weight reduction caused by the evaporation of water from the samples' surfaces. Diamagnetic behavior was observed in M-H hysteresis curves at room temperature.

Acknowledgements

The authors extend his appreciation and acknowledge the financial support through Researchers Supporting Project number (RSP2025R354), King Saud university, Riyadh, Saudi Arabia.

References

[1] Ishak, NAI Md, S. K. Kamarudin, S. N. Timmiati, Materials Research Express 6, no. 11 (2019): 112004; https://doi.org/10.1088/2053-1591/ab4458

[2] Annu, Ali A., Shakeel Ahmed, Handbook of Ecomaterials 2018 (2018): 1-45. https://doi.org/10.1007/978-3-319-48281-1_115-1

[3] Soltys, Liubov, Ostap Olkhovyy, Tetiana Tatarchuk, Mu Naushad, Magnetochemistry 7, no. 11 (2021): 145; https://doi.org/10.3390/magnetochemistry7110145

[4] Shafey, Asmaa Mohamed El, Green Processing and Synthesis 9, no. 1 (2020): 304-339; https://doi.org/10.1515/gps-2020-0031

[5] Priya, Naveen, Kamaljit Kaur, Amanpreet K. Sidhu, Frontiers in Nanotechnology 3 (2021): 655062; https://doi.org/10.3389/fnano.2021.655062

[6] Bukhari, Aysha, Irfan Ijaz, Ezaz Gilani, Ammara Nazir, Hina Zain, Ramsha Saeed, Saleh S. Alarfaji, Sajjad Hussain, Rizwana Aftab, Yasra Naseer, Coatings 11, no. 11 (2021): 1374; https://doi.org/10.3390/coatings11111374

[7] Jeevanandam, Jaison, Siaw Fui Kiew, Stephen Boakye-Ansah, Sie Yon Lau, Ahmed Barhoum, Michael K. Danquah, João Rodrigues, Nanoscale 14, no. 7 (2022): 2534-2571; https://doi.org/10.1039/D1NR08144F

[8] M. Sundararajan, J. Vidhya, R. Revathi, M. Sukumar, B. Arunadevi, R. Rajkumar, S. Ramachandran, M. Kamalakannan, Chandra Sekhar Dash, Jothi Ramalingam Rajabathar, SelvarajAroykaraj, Inorg. Nano-Met. Chem.

[9] B. Chavillon, L. Cario, A. Renaud, F. Tessier, F. Cheviré, M. Boujtita, Y. Pellegrin, E. Blart, A. Smeigh, L. Hammarstrom, F. Odobel, J. Am. Chem. Soc., 134 (2011) 464-70; https://doi.org/10.1021/ja208044k

[10] R. Jothiramalingam, T. Radhika, N.P. Kavitha, H. Al-Lohedan, D.M. Aldhayan, M. Karnan, Dig. J. Nanomater. Biostructures. 19 (2024) 15–24. https://doi.org/10.15251/DJNB.2024.191.15.

[11] J.R. Rajabathar, R. Thankappan, A. Sutha, H. Al-Lohedan, A. Mahmoud Karami, S. Ashok Kumar, G. Devendrapandi, S. Roji Marjorie, R. Balu, Opt. Mater. (Amst). 148 (2024). https://doi.org/10.1016/j.optmat.2023.114820 .

[12] M Schumm, M Koerdel, S Müller, H Zutz, C Ronning, J Stehr, D M Hofmann, J Geurts, New J. Phys.10 (2008) 043004; https://doi.org/10.1088/1367-2630/10/4/043004

[13] J. Lang, J. Wang, Q. Zhang, X. Songsong, Q. Han, Y. Zhang, Hongju. Zhai, J. Cao, Y. Yan, J. Yang, Chem. Res. Chin. Univ. 30 (2014) 538-542; https://doi.org/10.1007/s40242-014-4028-8

[14] A. Bechen, M. Durr, L.P. Nostro, P. Baglioni, J. Nanoparticle Res. 10 (2008) 679-689; https://doi.org/10.1007/s11051-007-9318-3